Advanced Processing Sequence for 3-D THz Imaging

Hugo Balacey, Benoit Recur, Jean-Baptiste Perraud, Joyce Bou Sleiman, Jean-Paul Guillet, and Patrick Mounaix

Abstract—**In this paper, we present an advanced image processing sequence to perform nondestructive inspection from 3-D terahertz (THz) images. We develop all the steps starting from a 3-D tomographic reconstruction of a sample from radiographs acquired with a monochromatic millimeter-wave imaging system to an automated segmentation, extracting the different volumes of interest (VOI) composing the sample. This leads to 3-D visualization and dimensional measurements. This inspection is completed by a skeletonization and caliber analysis providing an accurate assessment of the structure, geometry, and morphology of the acquired object. Overall sequence is implemented onto an unique software and validated through different sample analysis.**

Index Terms—**Caliber analysis, nondestructive testing, processing sequence, segmentation, skeletonization, THz tomography.**
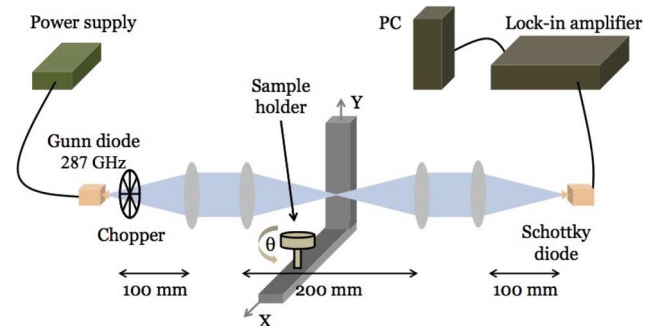

Fig. 1. Experimental setup: a Gunn diode delivers a THz wave with a power of 12 mW at 287 GHz. The THz beam is collimated and focused with a pair of PTFE lenses. The acquired sample is positioned on a three-axes motorized stage comprising the X, Y, and θ movements.

I. INTRODUCTION

CONTINUOUS-WAVE terahertz computed tomography (CW-THz CT) is an emerging technique providing 3-D visualization of an object from its set of radiographs acquired at different viewing angles [1]–[10]. The low absorption and large penetration depth of transmitted THz wave (usually between 0.1 and 4 THz) lead to a local contrast allowing the reconstruction of volumes imaging the internal structure of transparent objects. Since these materials (such as plastics, wood, or paper) are troublesome to inspect with other tomographic techniques such as X-rays [11], 3-D THz tomography is paving the route to new applications in nondestructive testing (NDT) [12], explosive or illicit drug detection thanks to spectroscopy capabilities [13], [14], art conservation [15], [16] or biomedical imaging research [17].

Even if some experiments have been performed to tackle these specific applications, no processing sequence has been proposed to our own knowledge to provide a complete and automated structural and dimensional analysis, in 3-D, from THz data. Thus in this paper we focus on the analyze capabilities from 3-D reconstructed volumes obtained by a CW-THz imaging system (that could be extended to spectroimaging with a pulsed system). We aim at demonstrating that images obtained by such a setup are compatible with an automated processing composed of: 1) an *ad-hoc* segmentation, extracting

the sample from the background and reconstruction noise [18]; 2) a component labelling, which separates the different regions of interest (ROI) [19]; 3) a skeletonization, providing additional meta-data about the sample morphology; and 4) a caliber tracking that automatically measures distance distributions between skeletons and ROIs.

The remainder of the paper is organized as follows. Section II describes the experimental setup acquiring radiographs and the tomographic reconstruction algorithm computing 3-D volumes of scanned objects. Then, in Section III, we detail the segmentation, component labelling, skeletonization, and caliber tracking tool giving dimensional and geometrical information about the object structure. Before concluding, the capability of the overall processing sequence, as well as the current limitation of THz devices, are discussed in Section IV.

II. 3-D CW-THz TOMOGRAPHY

This section details the homemade THz scanner and the 3-D THz tomographic reconstruction algorithm used in this work.

A. Experimental Setup

Our experimental setup is a 3-D millimeter-wave tomographic scanner (see Fig. 1). To generate the millimeter-wave, a Gunn diode, the WAX3 from "Wasa MilliMeter Wave" is used and coupled to a frequency tripler. It has an output frequency range of 261–315 GHz and delivers 12 mW at $\nu = 287$ GHz. It is employed with an additional horn antenna and is adapted to be used for phase-locked or frequency-locked sources. After generation, the THz beam is collimated and focussed by a pair of Polytetrafluoroethylene (PTFE) lenses (focal length is $f = 50$ mm and the diameter is $D = 50.8$ mm). The sample is positioned on a motorized stage comprising X,Y translations and θ rotation around Y-Axis. Detection is performed by a

H. Balacey and B. Recur are with Noctylio S.A.S, 33000 Bordeaux, France (e-mail: hugo.balacey@noctylio.com; benoit.recur@noctylio.com).

J.-B. Perraud, J. B. Sleiman, J.-P. Guillet, and P. Mounaix are with the IMS, BAT A31, CNRS UMR 5812, 33405 Talence, France.

Fig. 2. (a) Acquired sample: a correct-it roller. (b) Radiographs along $N_\theta = 36$ projections uniformly distributed between 0 and 180°.

zero-bias Schottky diode WR3.4 from "Virgina Diodes,, modulated at 1 kHz by a mechanical chopper and combined with a lock-in amplifier. The NEP of the diode is 17.6 pW/$\sqrt{\text{Hz}}$. The dynamic range of the lock-in amplifier (Stanford Research System SR830) is more than 100 dB, but once set to caliber, the range is limited to 40 dB. The diode detects in the range of 220–330 GHz and has a response time of several nanoseconds. However, lock-in amplifier limits the speed at 50 ms per point due to modulation.

A 2-D radiograph is measured by moving the object along the X and Y axes (isometric scan step usually between 0.5 and 1 mm). Then, the sample is rotated to measure a set of radiographs at different viewing angles. A complete acquisition consists of N_θ projections distributed around 180° with a uniform angle step of $\delta_\theta = 180°/N_\theta$. For instance, Fig. 2(b) shows the acquisition of $N_\theta = 36$ projections ($\delta_\theta = 5°$) sized 148×120 pixels (translation step of 1 mm) of the correct-it roller shown in Fig. 2(a). At this projection size, the acquisition time is approximately 9 min/projection.

B. Tomographic Reconstruction

The projection set is processed by a tomographic algorithm to reconstruct a 3-D volume (denoted tomogram) imaging the scanned object. In the tomogram, the 3-D structure of the sample is revealed thanks to proportionality between the intensity of each reconstructed voxel with the overall attenuation encountered by the THz radiation at the corresponding position in the sample. In the THz range, this attenuation is mainly proportional to the extinction coefficient (neglecting optical effects). Several reconstruction techniques have been proposed during the last decades, especially in the field of X-ray tomography for medical imaging [20]–[29]. Meanwhile, a few have been investigated for THz tomography [1]–[7], [30]. In this paper, we use a regularized 3-D implementation of the THz ordered subsets convex (THz-OSC) algorithm [9].

THz-OSC is an iterative process following superiterations t and sub-iterations s. Each subiteration updates the volume under reconstruction, μ_s^t, from a subset of projections denoted $S(s)$. Each acquired projection, denoted R, is used only once per superiteration. The volume obtained after a sub-iteration s is used as starting volume of the next subset $s+1$. A main iteration t is completed when all subsets have been processed. The update of a voxel j of the volume is performed as follows:

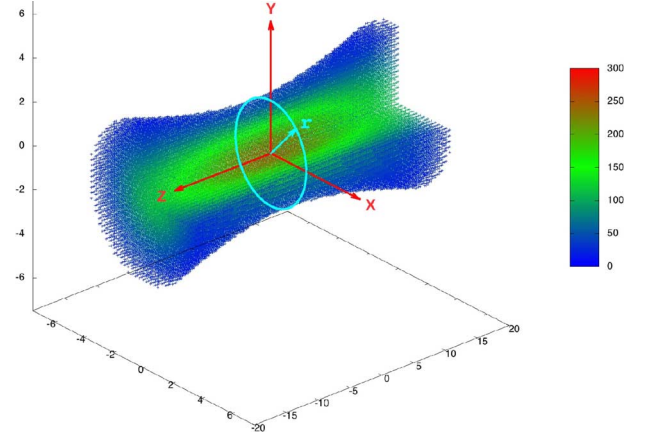$$\mu_{s+1}^t(j) = \mu_s^t(j) + \Delta_s^t(j)$$

Fig. 3. Beam propagation of the 287-GHz source. The light blue circle represents the beam shape at beam-waist with radius $r = 2.3$ mm (FWHM) according to measured beam-waist of our experimental setup. The color scale proportional to the beam intensity (a.u.). X, Y and Z axes scales in mm.

where

$$
\Delta_s^t(j)
$$
$$
= \frac{\displaystyle\sum_{i \in S(s)} w_{ij} \left[\hat{R}_s^t(i) - R(i)\right] - \beta \sum_{k \in \mathcal{N}(j)} y_{jk} \Phi'\left[\mu_s^t(j) - \mu_s^t(k)\right]}{\displaystyle\sum_{i \in S(s)} w_{ij} \left(\sum_l w_{il}\right) \hat{R}_s^t(i) + \beta \sum_{k \in \mathcal{N}(j)} y_{jk} \Phi''\left[\mu_s^t(j) - \mu_s^t(k)\right]}
$$

$$(1)$$

where $w_{..}$ is a weight coefficient proportional to the voxel contribution on the detector, $y_{..}$ is a neighborhood weight factor (usually inverse proportional to the distance between both voxels), $\hat{R}_s^t(i)$ is the expected intensity computed from the previous volume estimate, μ_s^t, using a forward projection model, β is the relaxation parameter of the regularization term, $\Phi'(\cdot)$ and $\Phi''(\cdot)$ are, respectively, the first and second derivative of the potential function $\Phi(\cdot)$ regularizing the solution, and $\mathcal{N}(j)$ is the neighborhood of pixel j. The forward projection model used in this work is

$$\hat{R}_s^t(i) = I_0(i)\mathrm{e}^{-\sum_j w_{ij}\mu_s^t(j) \star G(j)} + bg(i) \qquad (2)$$

where I_0 is the maximal intensity, bg is the background noise, $\star$ is the convolution operator, and $G(j)$ is the Gaussian propagation model of the THz beam [9]. For instance, Fig. 3 shows the measured and then analytically modeled Gaussian intensity propagation of the 287-GHz source (Rayleigh length is about 55 mm). Including the Gaussian beam model in the forward
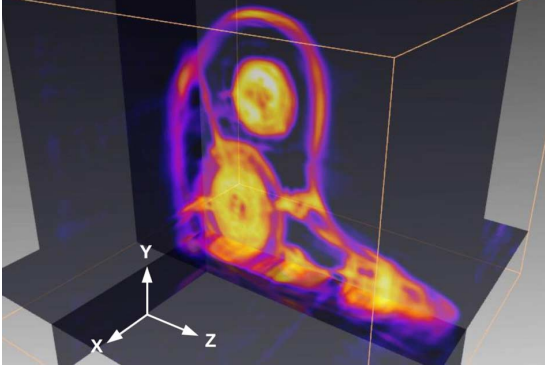
Fig. 4. Multiplanar rendering of the tomogram reconstructed by the penalized THz-OSC from the acquisition Fig. 2(b). It reveals in 3-D the internal mechanism of the correct-it roller.
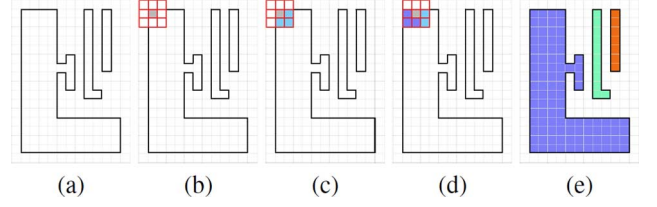

Fig. 5. (a) Binary mask resulting from segmentation is processed by a connected-component algorithm. (b) It runs through the image and creates a new label when a new component is detected. (c), (d) A pixel label remains the same while connected pixels are in the neighborhood of the next pixel of interest. (e) Three labels have been created at the end of the process.

projection model allows for correcting the blur effects caused by the nonlinear propagation of the wave through the sample. I_0 is quantified experimentally by lighting the detector with the source activated (without sample in between) and averaging the measured intensities. Similarly, the background noise bg is measured by averaging intensities measured when the THz source is inactive.

Finally, we use the LogCosh potential function $\Phi(x) = 2t^2 \log \cosh(|x|/t)$ to regularize the solution. It attenuates the small variations between neighborhood voxels, maximizing region homogeneity and it preserves edges beyond the given threshold t. For example, the regularized THz-OSC algorithm has been applied from the 36-projection set of the correct-it roller. Fig. 4 shows a 3-D multi-planar rendering of the reconstructed tomogram revealing the internal object mechanism.

III. ANALYSIS WORKFLOW

We develop now a complete analysis workflow from reconstructed tomograms. This processing sequence aims at providing structural, morphological and dimensional informations about the internal content of acquired samples. It is composed of a 3-D segmentation (separating the object from background and noise), followed by a component labelling (distinguishing the different ROIs in the object). These steps are respectively detailed in Sections III-A and III-B. We expect to compute dimensional data about each labelled ROI such as external surface area or 3-D dimension (in mm^3). The third step consists of a skeletonization of the ROIs in order to provide a structural model of the sample in a simple way (cf. Section III-C). The final workflow step (explained in Section III-D) is a caliber tracker measuring local dimensions along skeletons. This helps assessment and validation of object morphology.

A. Automated Segmentation Using the K-Mean Algorithm

We develop now the tomogram segmentation step that distinguishes the object from the other parts (air, noise, and artefacts). Several 3-D segmentation methods have been proposed during the last decades. Point-based techniques compare voxel intensities between each other to allocate regions according to voxel similarities, without *a priori* knowledge about regions or edges

[31]–[35]. Edge-based methods estimate contours between regions according to *a priori* edge properties [36]–[38]. Similarly, region-based techniques [39], [40] group voxels according to a region model. Apart from these image processing techniques, few methods segment the tomogram according to sample chemical properties but they imply ad-hoc acquisitions [41]–[44]. In our case, a point-based segmentation such as K-mean algorithm is the most dedicated approach to remove background and noise from the overall tomogram [35], [45]. K-mean is a very well-known clustering method, widely used in image processing and appreciated for its computational efficiency. Given a set of k means (randomly selected at first estimate), this iterative method partitions all the voxels into k sets and minimizes the within-cluster sum of squares:

$$\arg \min_{\mathbf{S}} \sum_{i=1}^{k} \sum_{\mathbf{x} \in S_i} \|x - \bar{x}_i\|^2 \tag{3}$$

where x is the voxel intensity, $S = \{S_i, i \in [1, k]\}$ is the cluster set and $\bar{x}_i$ is the average intensity of S_i. Thus optimal set of $\bar{x}_i$, $i \in [1, k]$, is estimated during the iterations. During our experiments, we have noticed that choosing $k = 3$ is often the best compromise between computation efficiency and result accuracy. It leads to three classes automatically separating the tomogram as follows. First, the class C_1 is composed of low-intensity voxels representing the air and background noise. Thus, the object of interest is represented by the two subsequent classes C_2 and C_3, corresponding, respectively, to the low- and high-intensity parts of the object. With $k = 2$, the segmentation usually merges as C_1 the background with the noise, but also some object details. Choosing $k > 3$ increases, the number of subclasses in C_1 and $C_2 \cup C_3$. It could be useful if the sample were composed of a larger number of very different attenuating materials, but this is often not the case in our experiments.

B. Component Labelling

The object cluster $C_2 \cup C_3$, denoted C_{sample} hereafter, can be viewed as a 3-D binary mask indicating which part of the tomogram corresponds to the object. This binary mask can be composed of several unconnected components we differentiate using a connected-component labelling algorithm [46]. A connected component of C_{sample} is a voxel subset of maximal size such that all of the voxels in C_{sample} are connected. Two voxels v_i and v_j are connected if there is a path of voxels $(v_0, v_1, v_2, \ldots, v_n)$ such that $v_0 = v_i$, $v_n = v_j$ and $\forall 1 \leq i \leq n$, v_{i-1} and v_i are neighbors. An example is given in Fig. 5.
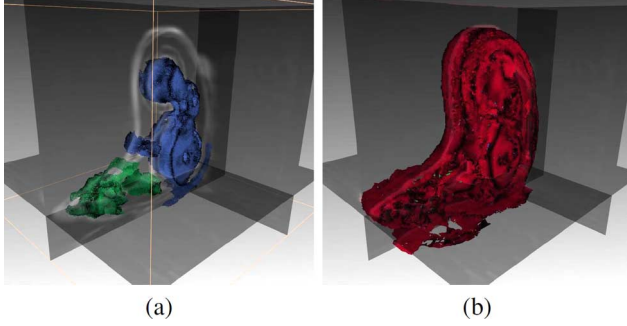
Fig. 6. The 3-D segmentation and component labelling of the tomogram imaging the correct-it roller leads to a 3-D mesh visualization of the different parts of the object: (a) mechanism of the ruban (blue) and head of the roller (green); (b) external surface made in plastics.

The tomogram of the correct-it roller is processed by the K-mean algorithm (with $k = 3$) and the connected-component labelling to obtain a set of volumes of interest (VOIs) composing the object. Fig. 6 shows the VOI meshing, revealing the internal volumes of the Ruban mechanism and the head of the roller. Segmented and labeled data allow to compute dimensional measurements as discussed in Section IV-A.

C. Skeletonization

Skeletonization is the processing performed on a VOI mask M that consists of determining the morphological graph of its shape. A skeleton is composed of: 1) a set $S = \{B_i, i \in [1, N_B]\}$ of connected branches (where N_B is the number of branches) and 2) a set $C = \{N_j, j \in [1, N_N]\}$ of nodes (where N_N is the number of nodes). A skeleton (S, C) verifies that, for each couple $(B_i, B_j) \in S^2$, there is a way going through a series of nodes in C and of branches in $S - \{B_i, B_j\}$ that connects B_i to B_j. Moreover, let us consider a point $p \in B_i$ and $\vec{n_p}$ as the tangent of the branch at this point. p is selected to be the baricenter of the overall set of connected points $E = \{p_i \in P_p, i \in \mathbb{N}\}$, such as E corresponds to the edges of M and the plane P_p is normal to $\vec{n_p}$. In this paper, we use a thinning approach to skeletonize segmented data and label branches and nodes [47]–[49]. It consists of: 1) iteratively eroding the shape of M until obtaining the thinnest structure and 2) estimating each point function (branch or node) in order to manage structure hierarchy. An example of skeletonization and hierarchy is provided on Fig. 7 from synthetic data.

D. Tubular Shape Tracking and Caliber Analysis

Thanks to the skeletonization and the set of orthonormal planes P_* extracted along the graph, we can compute several dimension statistics between a point p of the skeleton and the corresponding VOI edges included in the orthonormal plane. For example, we can measure the extremum or average diameters/distances, as well as the standard deviation of the distance between p and the VOI in order to get some meta-data related to the local morphology of the sample. Moreover, the skeletonization hierarchy allows one to perform such measurements all along a given branch in order to assess internal dimension homogeneity or to detect bottlenecks inside tubes, for instance. This capability is illustrated and discussed in Section IV-B.
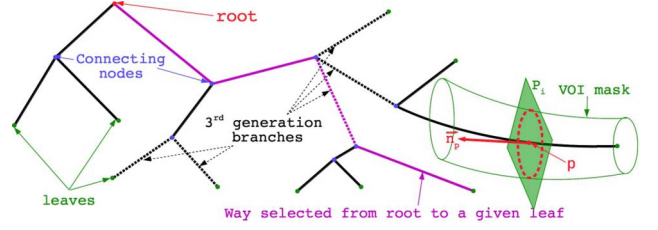

Fig. 7. Skeleton labelling: branches and nodes (root, connections, and leaves) between branches characterize the morphology of a given structure. Skeleton is computed by finding each point p, baricenter of a VOI mask along planes P_p such that P_p is normal to each corresponding vector $\vec{n_p}$, i.e., the tangent of the skeleton at position p. Synthetic data have been used in this example.
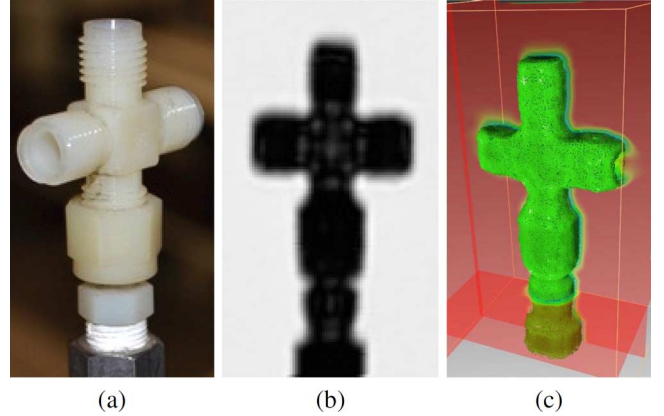

Fig. 8. (a) Photograph of the cross tube. (b) Radiograph of the sample at $\theta = 0°$. (c) 3-D meshed visualization (in wireframe mode) of reconstructed tomogram.

IV. APPLICATIONS AND DISCUSSION

Here, we apply the proposed analysis workflow to various samples. In Section IV-A, we demonstrate the efficiency of the processing sequence for quantitative and qualitative NDT. Then in Section IV-B, we discuss the skeletonization and tubular shape tracking and analysis from 3-D THz data. During our discussion, we also comment on current limitations mainly due to scanner properties.

A. Internal Inspection and Dimensional Measurements

We demonstrate now the capability of the processing sequence to measure surface or volume characteristics required for NDT. We discuss results according to THz radiation properties. This processing is applied on three samples for demonstration: 1) the correct-it roller; 2) a cross tube (see Fig. 8), and 3) a manual propipetter composed of a bulb and 3 valves: A, S, and E (see Fig. 9). They are acquired with $N_\theta = 36$ projections. The translational step is 1 mm (reconstructed voxel size of 1 mm^3) for the correct-it roller and the propipetter, and 0.5 mm (voxel size is 0.125 mm^3) for the cross-tube. Acquisition and reconstruction parameters are summarized for each sample on Table I. Tomograms are reconstructed with the regularized THz-OSC algorithm. Then, 3-D automated segmentation (using K-mean method with $k = 3$) and component labelling are performed to obtain VOIs composing the sample.
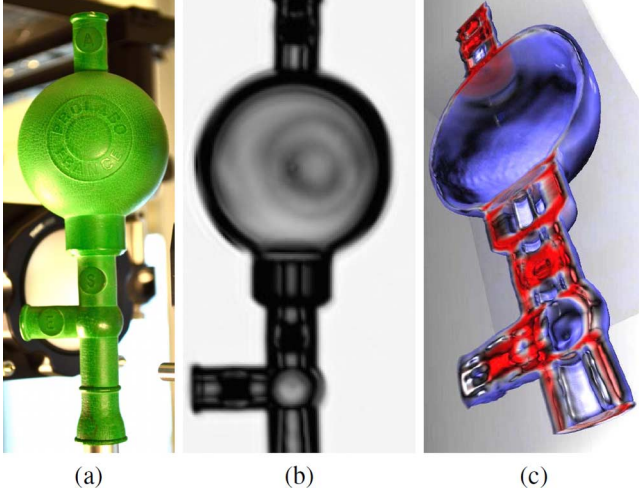
(a)   (b)   (c)

Fig. 9. (a) Photograph of the propipetter composed of a bulb and three valves A, S, and E. (b) Sample radiograph at $\theta = 0°$. (c) Volume rendering of the tomogram with an axial clipping reveals the internal composition of the object.
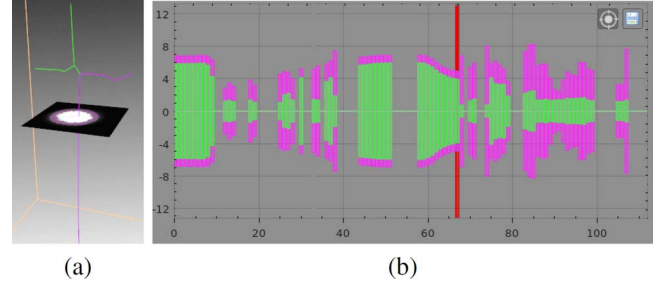

(a)   (b)

Fig. 10. (a) Skeleton of the cross tube overprinted on the multi-planar rendering of the sample. Caliber shape analysis is performed on the branch selected in purple. (b) Results of the caliber shape analysis. X-Axis: length; and Y-axis: dimension (in pixels, where 1 px = 0.5 mm according to acquisition/reconstruction resolution). In green: average diameter of the lumen inside the tube. In purple: average thickness of the tube wall. $x \in [0 \ldots 80]$ correspond to the vertical part of selected branch. $x \in [81 \ldots 112]$ is the horizontal part. Measures highlighted in red correspond to the visible slice on (a).

TABLE I

TOMOGRAPHY PARAMETERS. Δp: ACQUISITION STEP = RECONSTRUCTED VOXEL DIMENSION (IN mm). dim_{Acq}: DIMENSION OF THE ACQUISITION (IN NUMBER OF RADIOGRAPHS $N_\theta \times$ NUMBER OF ACQUIRED POINTS HORIZONTALLY AND VERTICALLY). T_{Acq}: ACQUISITION TIME (IN MIN). dim_V: RECONSTRUCTED VOLUME DIMENSION (IN Voxel^3)

Sample	Δp	dim_{Acq}	T_{Acq}	dim_V
Correct-it roller	1	$36 \times 148 \times 120$	320	$148 \times 148 \times 120$
Cross-tube	0.5	$36 \times 80 \times 140$	200	$80 \times 80 \times 140$
Propipetter	1	$36 \times 136 \times 260$	640	$136 \times 136 \times 260$

TABLE II

COMPONENT CHARACTERISTICS: MEAN AND STANDARD DEVIATION OF THE INTENSITY (A.U.), NUMBER OF POINTS AND FACES, AREA OF THE MESHED SURFACE (IN cm^2) AND VOLUME OF THE VOI (IN cm^3)

Sample	Mean	Std. Dev	points	faces	Area	Volume
Roller (Fig. 6)						
Blue	174.7	13.7	39336	63336	49.0	39.3
Green	162.0	24.4	8055	13189	10.2	8.1
Red	71.6	36.1	113752	193130	148.8	113.7
Tube (Fig. 8)	168.8	11.0	52664	83544	16.3	6.6
Prop. (Fig. 9)	49.5	85.1	361191	586206	458.7	361.2

Meta-data, such as the mean and standard deviation of the absorption, the number of points or the number of faces, the surface area, and the volume of each VOI, can be computed and measured with respect to the reconstructed volume resolution. All of these measures quantify locally the characteristics and properties of the object, as detailed in Table II. For instance, the average intensity value of the blue VOI of the correct-it roller is 174.67 (a.u., proportional to the absorption) and its standard deviation is 13.70. The area defining the green VOI is 10.23 cm^2 and the volume of the outer VOI is 113.75 cm^3.

Such surface and volume measurements only quantify the object VOIs which have been reconstructed from radiographs. Since THz waves suffer from multiple optical effects leading to signal losses [50]–[53], the overall contrast range increases and makes the contrast of low-absorption parts of the object negligible. Thus one has to keep in mind that void artefacts are omitted in the computation of surface and volume meta-data. Practically, very low intensity edges are confused with

background by the K-mean algorithm. As already notified in Section III-A, increasing number of classes so that $k \gg 3$ could solve the problem, but at the cost of computation time. Moreover the processing could no longer be automated. Another solution consists of increasing the number of acquired projections and/or acquiring along $360°$ instead of $180°$.

B. Skeletonization and Caliber Analysis of Samples

We discuss now the skeletonization and caliber analysis developed in Sections III-C and III-D. The VOI mask corresponding to the cross-tube is skeletonized by thinning method in order to obtain the graph of its structure, as shown on Fig. 10(a). The graph root is the bottom point of the skeleton. This skeleton is composed of $N_B = 5$ branches and $N_N = 6$ nodes (one root, two connections, and three leaves). Two branches define the horizontal arms of the cross-tube whereas two others define the vertical tubes. The fifth branch, in between the both connecting nodes, represents the intersection of horizontal and vertical tubes. The set of planes P_i normal to the skeleton are extracted from the overall volume. For instance, $P_{i=67}$ is shown in Fig. 10(a). According to the voxel dimension ($\Delta p = 0.5$ mm), this plane is positioned 33.5 mm from the root. Similarly, the overall length of the selected branch is 56 mm. Edge detection is applied on normal planes to measure distances from the skeleton to first and second edges of the mask. First-edge distance quantifies the diameter of the lumen of the tube (i.e., the hole diameter). The difference between second and first edge distances determines the thickness of the tube wall. The chart on Fig. 10(b) shows the average diameter of the tube hole (in green) and the average wall thickness along the branch selected in purple on Fig. 10(a). Measurements at each position where both lumen and wall-thickness are correctly extracted allow one to compute minimal, maximal, mean and standard deviation of diameters of the hole and wall thickness. For instance, in Table III, values computed from the tomogram are compared with the actual dimensions (directly measured from the object) for the selected plane $P_{i=67}$.

The tubular shape tracking is performed in a similar fashion from the tomogram of the propipetter (see Fig. 11). Internal shape of the bulb is clearly identified between planes $P_{i=45}$ and $P_{i=150}$. The mechanisms of valves A and S, which can be

TABLE III
DIMENSIONS: MINIMAL, MAXIMAL, AVERAGE AND STANDARD DEVIATION
(σ) OF THE HOLE DIAMETER, d, AND TUBE THICKNESS, th, FOR THE PLANE
$P_{i=67}$ (IN MM). R: ACTUAL DIMENSIONS DIRECTLY MEASURED AT THE
SAME POSITION FROM THE SAMPLE

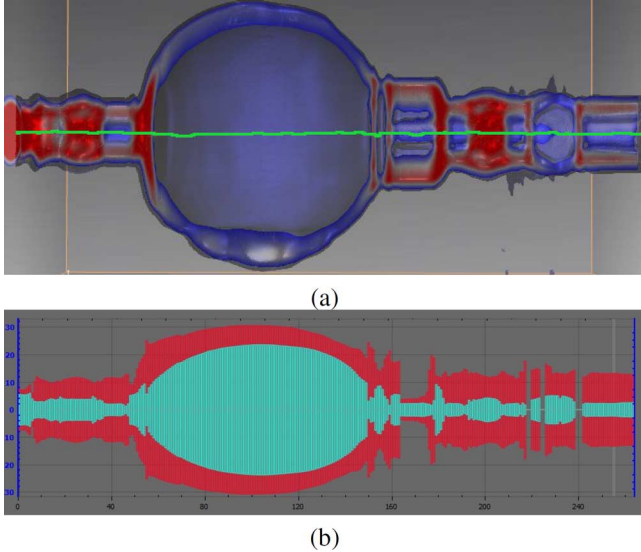|	R	min	max	A	σ
d	5	6.70	8.6	7.68	0.17
th	2.1	0	1.4	0.27	0.8

(a)

(b)

Fig. 11. (a) Main branch of the skeleton of the propipetter overprinted (in green) on the central cross-sectioned volume rendering of the sample. (b) Results of the caliber shape analysis performed along the selected branch. X-axis: length; Y-axis: dimension (in pixels, where 1 px = 1 mm according to acquisition/reconstruction resolution). In green: average diameter of the lumen inside the tube. In red: average thickness of the propipetter wall.

tracked on the selected skeleton branch, are between $P_{i=15}$ and $P_{i=31}$ (for A), and $P_{i=190}$ and $P_{i=205}$ (for S).

One can remark that shape tracking is not found at some points. For example, in Fig. 10(b), P_i, s.a. $i \in [38, 43]$ are not correctly analyzed. Similarly, in Fig. 11(b), tubular shape tracking is not processed for planes P_i, s.a. $i \in [239, 241]$. These errors result from bottlenecks (holes seem to be filled with undesired matter). However, due to the resolution limitation ($\lambda/2 \approx 0.5$ mm at 287 GHz) and knowing the different scattering effects encountered by THz waves, these results potentially illustrate a limitation of the scanning system for these samples. Several ways could be investigated to overcome this issue. First, the scanning system could be improved by using higher frequency source and detector with sufficient signal-to-noise ratio. Second, as already discussed in the previous section, an automatic tuning of the projection number and of the THz wave energy to the scanned sample could optimize obtained 3-D reconstruction.

V. CONCLUSION

In this paper, an analysis workflow has been developed to achieve efficient and automated qualitative and quantitative measurements from 3-D CW-THz acquisitions. A 3-D tomogram obtained by THz computerized tomography has been considered as input of this processing sequence.

First, the tomogram has been segmented and labelled into different VOIs to be analyzed separately. The 3-D visualization and surface or volume quantizations have been performed on several samples to illustrate non-destructive inspection capabilities of these steps. Then, a skeletonization has been applied on segmented data, extracting geometrical meta-data such as disposition and structure of the object, internal morphology and caliber dimensions. This processing has been applied on several tubular samples in order to assess their radius homogeneity along skeletons. During our experiment discussion, we also mentioned that the developed processing sequence could be used to optimize the acquisition to the sample under inspection.

Our future works will focus on the development of the regularized THz-OSC for reconstructing from multi-energy and/or multi-intensity acquisitions. We expect that such an approach could solve the hole artefacts observed on a given energy tomogram thanks to the other energy. Moreover, since tomographic reconstruction computes attenuation (or extinction) coefficients, a multi-energy approach could also be used to perform a segmentation based on chemical characteristics [41]–[44], as a complementary of the image-based K-mean method used in the current workflow. This prospect implies that we will have to: 1) investigate dual reconstruction/chemical-based segmentation and 2) make the forward process $\hat{R}$ computation more realistic with optical effects.

REFERENCES

[1] B. Ferguson, S. Wang, D. Gray, D. Abbot, and X.-C. Zhang, "T-ray computed tomography," *Opt. Lett.*, vol. 27, no. 15, pp. 1312–1314, 2002.

[2] S. Wang, B. Ferguson, D. Abbott, and X.-C. Zhang, "T-ray imaging and tomography," *J. Biolog. Phys.*, vol. 29, no. 2-3, pp. 247–256, 2003.

[3] S. Wang and X. Zhang, "Pulsed terahertz tomography," *J. Phys. D, Appl. Phys.*, vol. 37, no. 4, p. R1, 2004.

[4] M. Awad and R. Cheville, "Transmission terahertz waveguide-based imaging below the diffraction limit," *Appl. Phys. Lett.*, vol. 86, no. 22, 2005, Art. ID 221107.

[5] X. Yin, B. W.-H. Ng, B. Ferguson, and D. Abbott, "Wavelet based local tomographic image using terahertz techniques," *Digital Signal Process.*, vol. 19, no. 4, pp. 750–763, 2009.

[6] A. Brahm, M. Kunz, S. Riehemann, G. Notni, and A. Tünnermann, "Volumetric spectral analysis of materials using terahertz-tomography techniques," *Appl. Phys. B*, vol. 100, no. 1, pp. 151–158, 2010.

[7] B. Recur *et al.*, "Propagation beam consideration for 3d THz computed tomography," *Opt. Exp.*, vol. 20, no. 6, pp. 5817–5829, 2012.

[8] B. Recur, H. Balacey, and P. Mounaix, "Expectation maximisation algorithms for terahertz transmission tomography," in *Proc. SPIE Opt. Eng.+ Applicant.*, 2014, Art. no 919900.

[9] B. Recur *et al.*, "Ordered subsets convex algorithm for 3d terahertz transmission tomography," *Opt. Exp.*, vol. 22, no. 19, pp. 23299–23309, 2014.

[10] J. P. Guillet *et al.*, "Review of terahertz tomography techniques," *J. Infrared, Millimeter, and Terahertz Waves*, vol. 35, no. 4, pp. 382–411, 2014.

[11] W. L. Chan, J. Deibel, and D. M. Mittleman, "Imaging with terahertz radiation," *Rep. Progr. Phys.*, vol. 70, no. 8, p. 1325, 2007.

[12] F. Ospald *et al.*, "Aeronautics composite material inspection with a terahertz time-domain spectroscopy system," *Opt. Eng.*, vol. 53, no. 3, 2014, Art. ID 031208.

[13] K. Kawase, Y. Ogawa, Y. Watanabe, and H. Inoue, "Non-destructive terahertz imaging of illicit drugs using spectral fingerprints," *Opt. Exp.*, vol. 11, no. 20, pp. 2549–2554, 2003.

[14] Y. Shen, T. Lo, P. Taday, B. Cole, W. Tribe, and M. Kemp, "Detection and identification of explosives using terahertz pulsed spectroscopic imaging," *Appl. Phys. Lett.*, vol. 86, no. 24, 2005, Art. ID 241116.

[15] K. Fukunaga and M. Picollo, "Terahertz spectroscopy applied to the analysis of artists? materials," *Appl. Phys. A*, vol. 100, no. 3, pp. 591–597, 2010.

[16] P. Mounaix, A. Younus, J.-C. Delagnes, E. Abraham, L. Canioni, and M. Fabre, "Spectroscopy and terahertz imaging for sigillography applications," *J. Eur. Opt. Soc.–Rapid Publications*, vol. 6, 2011.

[17] S. Huang, Y. Wang, D. Yeung, A. Ahuja, Y. Zhang, and E. Pickwell-MacPherson, "Tissue characterization using terahertz pulsed imaging in reflection geometry," *Phys. Med. Biol.*, vol. 54, no. 1, p. 149, 2009.

[18] J. P. Guillet *et al.*, "Low-frequency noise effect on terahertz tomography using thermal detectors," *Appl. Opt.* vol. 54, no. 22, pp. 6758–6762, Aug. 2015 [Online]. Available: http://ao.osa.org/abstract.cfm?URI=ao-54-22-6758

[19] H. Balacey, J.-B. Perraud, J. B. Sleiman, J.-P. Guillet, B. Recur, and P. Mounaix, "Processing sequence for non-destructive inspection based on 3d terahertz images," in *Proc. SPIE/COS Photon. Asia*, 2014, Art. ID 92750J.

[20] L. A. Shepp and Y. Vardi, "Maximum likelihood reconstruction for emission tomography," *IEEE Trans. Med. Imaging*, vol. MI-1, no. 2, pp. 113–122, Oct. 1982.

[21] K. Lange and R. Carson, "EM reconstruction algorithms for emission and transmission tomography," *J. Comput. Assisted Tomography*, vol. 8, no. 2, pp. 306–316, 1984.

[22] A. Andersen and A. C. Kak, "Simultaneous algebraic reconstruction technique (SART): A superior implementation of the art algorithm," *Ultrason. Imaging*, vol. 6, no. 1, pp. 81–94, 1984.

[23] K. Lange, M. Bahn, and R. Little, "A theoretical study of some maximum likelihood algorithms for emission and transmission tomography," *IEEE Trans. Med. Imaging*, vol. MI-6, no. 2, pp. 106–114, Jun. 1987.

[24] H. M. Hudson and R. S. Larkin, "Accelerated image reconstruction using ordered subsets of projection data," *IEEE Trans. Med. Imaging*, vol. 13, no. 4, pp. 601–609, Dec. 1994.

[25] K. Lange and J. A. Fessler, "Globally convergent algorithms for maximum a posteriori transmission tomography," *IEEE Trans. Image Process.*, vol. 4, no. 10, pp. 1430–1438, Oct. 1995.

[26] J. A. Fessler, "Hybrid Poisson/polynomial objective functions for tomographic image reconstruction from transmission scans," *IEEE Trans. Image Process.*, vol. 4, no. 10, pp. 1439–1450, Oct. 1995.

[27] B. D. Man *et al.*, "A study of four minimization approaches for iterative reconstruction in X-ray CT," in *IEEE Nuclear Sci. Symp. Conf. Rec.*, 2005, vol. 5, pp. 2708–2710.

[28] C. Kamphuis and F. J. Beekman, "Accelerated iterative transmission CT reconstruction using an ordered subsets convex algorithm," *IEEE Trans. Med. Imaging*, vol. 17, no. 6, pp. 1101–1105, Dec. 1998.

[29] H. Erdogan and J. A. Fessler, "Ordered subsets algorithms for transmission tomography," *Phys. Med. Biol.*, vol. 44, no. 11, p. 2835, 1999.

[30] B. Recur *et al.*, "Investigation on reconstruction methods applied to 3d terahertz computed tomography," *Opt. Exp.*, vol. 19, no. 6, pp. 5105–5117, 2011.

[31] T. Ridler and S. Calvard, "Picture thresholding using an iterative selection method," *IEEE Trans. Syst., Man Cybern.*, vol. SMC-8, no. 8, pp. 630–632, Aug. 1978.

[32] O. D. Trier and A. K. Jain, "Goal-directed evaluation of binarization methods," *IEEE Trans. Pattern Anal. Mach. Intell.*, vol. 17, no. 12, pp. 1191–1201, Dec. 1995.

[33] V. A. Epanechnikov, "Non-parametric estimation of a multivariate probability density," *Theory of Probability Applicant.*, vol. 14, no. 1, pp. 153–158, 1969.

[34] T. Denoeux, "A K-nearest neighbor classification rule based on Dempster-Shafer theory," *IEEE Trans. Syst., Man Cybern.*, vol. 25, no. 5, pp. 804–813, May 1995.

[35] J. MacQueen *et al.*, "Some methods for classification and analysis of multivariate observations," in *Proc. 5th Berkeley Symp. Math. Statist. and Probability*, Berkeley, CA, USA, 1967, vol. 1, pp. 281–297.

[36] S. W. Zucker and R. A. Hummel, "A three-dimensional edge operator," *IEEE Trans. Pattern Anal. Mach. Intell.*, vol. PAMI-3, no. 3, pp. 324–331, Mar. 1981.

[37] J. Serra, *Image Analysis and Mathematical Morphology*. New York, NY, USA: Academic, 1982, vol. 1.

[38] M. Kass, A. Witkin, and D. Terzopoulos, "Snakes: Active contour models," *Int. J. Comput. Vis.*, vol. 1, no. 4, pp. 321–331, 1988.

[39] S. L. Horowitz and T. Pavlidis, "Picture segmentation by a directed split-and-merge procedure," in *Proc. 2nd Int. Joint Conf. Pattern Recognition*, 1974, vol. 424, p. 433.

[40] I. Manousakas, P. Undrill, G. Cameron, and T. Redpath, "Split-and-merge segmentation of magnetic resonance medical images: Performance evaluation and extension to three dimensions," *Comput. Biomed. Res.*, vol. 31, no. 6, pp. 393–412, 1998.

[41] R. E. Alvarez and A. Macovski, "Energy-selective reconstructions in X-ray computerised tomography," *Phys. Med. Biol.*, vol. 21, no. 5, p. 733, 1976.

[42] S. Siddiqui and A. A. Khamees, "Dual-energy CT-scanning applications in rock characterization," in *Proc. SPE Ann. Tech. Conf. and Exhibition*, Houston, TX, USA, 2004, Paper SPE-90520-MS.

[43] B. Heismann, J. Leppert, and K. Stierstorfer, "Density and atomic number measurements with spectral X-ray attenuation method," *J. Appl. Phys.*, vol. 94, no. 3, pp. 2073–2079, 2003.

[44] B. Recur, M. Paziresh, G. Myers, A. Kingston, S. Latham, and A. Sheppard, "Dual-energy iterative reconstruction for material characterisation," in *Proc. SPIE Opt. Eng. + Applicant.*, 2014, Art. ID 921213.

[45] J. A. Hartigan and M. A. Wong, "Algorithm as 136: A K-means clustering algorithm," *Appl. Statist.*, pp. 100–108, 1979.

[46] H. Samet and M. Tamminen, "Efficient component labeling of images of arbitrary dimension represented by linear bintrees," *IEEE Trans. Pattern Anal. Mach. Intell.*, vol. 10, no. 4, pp. 579–586, Apr. 1988.

[47] T.-C. Lee, R. L. Kashyap, and C.-N. Chu, "Building skeleton models via 3-d medial surface axis thinning algorithms," *CVGIP: Graphical Models and Image Processing*, vol. 56, no. 6, pp. 462–478, 1994.

[48] K. Mori, J.-I. Hasegawa, Y. Suenaga, and J.-I. Toriwaki, "Automated anatomical labeling of the bronchial branch and its application to the virtual bronchoscopy system," *IEEE Trans. Med. Imaging*, vol. 19, no. 2, pp. 103–114, 2000.

[49] H. Balacey, G. Dournes, P. Desbarats, M. Montaudon, J.-P. Domenger, and F. Laurent, "A new processing sequence to assess airways using 3d CT-scan," in *Proc. ICIP*, 2013, pp. 2339–2343.

[50] E. Abraham, A. Younus, C. Aguerre, P. Desbarats, and P. Mounaix, "Refraction losses in terahertz computed tomography," *Opt. Commun.*, vol. 283, no. 10, pp. 2050–2055, 2010.

[51] E. Hérault, M. Hofman, F. Garet, and J.-L. Coutaz, "Observation of terahertz beam diffraction by fabrics," *Opt. Lett.*, vol. 38, no. 15, pp. 2708–2710, 2013.

[52] Y.-D Li, Q. Li, J.-Y. She, and Q. Wang, "Investigation on diffraction characteristics of continuous terahertz beam limited by hard-edge apertures," *Optik-Int. J. for Light and Electron Opt.*, vol. 124, no. 22, pp. 5669–5673, 2013.

[53] A. Brahm, A. Wilms, M. Tymoshchuk, C. Grossmann, G. Notni, and A. Tünnermann, "Optical effects at projection measurements for terahertz tomography," *Opt. & Laser Technol.*, vol. 62, pp. 49–57, 2014.

Hugo Balacey received the Ph.D. degree in computer science from the University of Bordeaux, Bordeaux, France, in 2013.

Then, he joined the LOMA laboratory, UMR CNRS 5298, in 2014 as a Post-Doctoral Fellow to work on automatic processing sequences for THz image acquisition and processing. He is now working at IMS (UMR CNRS 5218) on cancerous tissue analysis using THz spectro-imaging. He recently co-founded the start-up company Noctylio, Bordeaux, France, implementing 3-D and multispectral analysis software. His main interests include segmentation and skeletonization of the bronchial tree, management of 3-D volumes, and 2-D/3-D representation over time for medical applications.

Benoit Recur received the M.S. degree and Ph.D. degree in computer science from the University of Bordeaux, Bordeaux, France, in 2007 and 2010, respectively.

Then, he joined at the Waves and Materials Laboratory of Aquitaine, LOMA UMR CNRS 5798, Bordeaux, France, and the Research School of Physics and Engineering (RSPE), Australian National University, Canberra, Australia. He is currently with INSERM U1029 (French Institute of Health and Medical Research). His research area focuses on the conception and development of high-resolution and/or multi-spectral 3-D imaging techniques based on X-Ray, Infrared and/or THz waves, with applications to medical and material science and non-destructive testing. He recently cofounded the start-up company Noctylio, Bordeaux, France, implementing 3-D and multispectral analysis software.

Jean Baptiste Perraud was born on December 24, 1987. He received the M.S. degree in aeronautical maintenance engineering from "Institut de Maintenance Aéronautique" in 2011, and the M.S. degree in physics from the University of Bordeaux, Bordeaux, France, in 2013. He is currently working toward the Ph.D. degree at IMS, UMR 5218, Talence, France.

During his internship at "Laboratoire Ondes et Matière d'Aquitaine" (LOMA) UMR 5798, on the SLAM team, he worked for the development of nondestructive test (NDT) of aeronautical composite multilayered structure using terahertz spectro-imaging (DOTNAC Project). Then, he was an Engineer with the SLAM team at LOMA working on development of terahertz spectro-imaging in the InPoSec Project. His doctoral work involved the project "Reconstruction Rapide d'images en régime terahertz 3-D (3R3D) (Fast 3-D terahertz imaging reconstruction). This project aims at demonstrating the feasablity of 2-D and 3-D scan samples with terahertz radiation in real time.

Joyce Bou Sleiman was born in Lebanon in 1989. She received the B.S. degree in general physics and M.S. degree in laser and medical applications from the Lebanese University, Beirut, Lebanon, in 2009 and 2011, respectively. She is currently working toward the Ph.D. degree at the CNRS (UMR 5218), Talence, France.

During her graduate work, she fulfilled her training at the University of Lille, France, at the PC2A laboratory to studying HAP in flames using laser diagnostics. In April 2013, she joined the CNRS (UMR 5218), University of Bordeaux, to establish her Ph.D. in the terahertz domain. Her research topic concerns terahertz imaging and spectroscopy for security application, in particularly, postal chain security in the InPoSec project. Parallel to her doctoral studies, she had a teaching experience at the University of Bordeaux during 2014–2015.

Miss Bou Sleiman is a member of the SPIE and OSA Student Chapters of Bordeaux. She was the recipient of the Best Student Paper Presentation during the SPIE Defense and Security Conference, Toulouse, France, in 2015.

Jean Paul Guillet was born in Lyon, France, in 1984. He received the M.Sc. and Ph.D. degrees from IES Lab, Montpellier, France, in 2007 and 2010, respectively, both in terahertz imaging.

The topic of this first research work was terahertz near-field microscopy using electronics-based components. During his postdoctoral studies, until 2013, his research focused on imaging and tomography, using femtosecond pulses, frequency-modulated continuous-wave approach, and a terahertz camera. He was an Associate Professor with the University of Bordeaux in 2013, at IMS (UMR CNRS 5218), where he is now focusing on very large-scale integration circuits fault isolation laser techniques and terahertz imaging.

Patrick Mounaix received the degree of engineer of Material Science from the Ecole Universitaire D'Ingénieur de Lille (EUDIL), in 1988, and the Ph.D. degree in quantum devices from the University of Lille, Lille, France, in 1992.

Then, he joined CNRS and the High Frequency Department of the Institut d'Electronique et de Micro-électronique du Nord (IEMN UMR 8520). He moved to Bordeaux in 2002 where he developed terahertz spectroscopy and imaging activities. Now, he is a Senior Researcher with IMS UMR CNRS 5218, Bordeaux University, and he is currently interested in equilibrium and time-resolved terahertz spectroscopy techniques for solid and liquid materials and 3-D terahertz imaging applications chiefly 3-D computed tomography for art science and NDE industrial applications. He works also on all dielectric metamaterials and their applications at microwave and terahertz frequency range. He has coauthored more than 180 papers.